International Journal of Fatigue 142 (2021) 105922

Contents lists available at ScienceDirect

International Journal of Fatigue

journal homepage: www.elsevier.com/locate/ijfatigue

A dual-imaging framework for multi-scale measurements of fatigue crack evolution in metallic materials

Susheel Dharmadhikari[a], Eric Keller[a], Asok Ray[a,b], Amrita Basak[a,*]

[a] Department of Mechanical Engineering, The Pennsylvania State University, University Park, PA 16802, United States
[b] Department of Mathematics, The Pennsylvania State University, University Park, PA 16802, United States

ARTICLE INFO

Keywords:
Fatigue
Short crack initiation
Short crack propagation
Long crack propagation
Al 7075-T6
Confocal microscope
Digital microscope

ABSTRACT

This paper presents a dual-imaging methodology to investigate fatigue crack initiation & propagation along the lateral and transverse directions in Al7075 flat specimens having a one-sided V-notch. The framework consists of a confocal and a digital microscope. The confocal microscope can detect the short crack initiation at a length-scale of 3 μm while the digital microscope has the capability of reliably measuring cracks at a scale of 0.5 mm. The apparatus provides a unique advantage of characterizing the multi-scale fatigue crack evolution without any significant restrictions on maximum specimen size and maximum loading or frequency.

1. Introduction

Fatigue is the weakening of a structure caused by cyclic loadings much below the ultimate tensile strength of the material. Such periodic weakening results in progressive damage to the structures leading to failures [1]. Despite several studies investigating the fatigue phenomenon since the 1800s, it remains to be one of the most enigmatic behaviors with failures occurring as late as 2010s [2]. This is due to the complex mechanisms involving multiple length- and time-scales, as well as the presence of several accounted and unaccounted operational factors, outlined elaborately in the existing literature [3,4]. The state-of-the-art fatigue failure analysis depends heavily on experimental investigations to evaluate the failure mechanisms in structural materials [3,4]. While model-based computational approaches (e.g., crystal plasticity [5]) continue to evolve and, are used to augment the fundamental understanding of fatigue damage evolution, these models are notoriously difficult to calibrate across a range of processing parameters and materials. The calibration difficulties are primarily because of the inadequacy in capturing the dynamical behavior of fatigue damage at the grain level due to the presence of random microstructural flaws and defects [6].

The entire time span of a fatigue crack evolution can be broken into two main phases: crack initiation and crack propagation, as shown in Fig. 1 [7]. Most of the traditional fatigue crack measurement techniques, prevalent in the current literature, focus on detecting the region between the short and long crack propagation because of the availability of feasible measurement techniques [8,9]. However, as illustrated in Fig. 1, it is critical to assess the fatigue life in the short crack initiation phase due to its markedly significant impact on the damage evolution in the long crack phase [10]. An important impetus to further the research in this field, therefore, is focused on the development of novel measurement techniques that can capture the crack initiation and propagation phenomena in the short crack regime. Due to the significant length-scale differences between the short and long crack initiation & propagation, the methods for measurements are also poles apart in terms of the complexity of measurement devices. For the long crack (initiation & propagation) regimes, optical and digital microscopes are adequate to capture the requisite data reliably [8,11]. However, for the short crack regimes, several innovative approaches have been reported in the open literature. In the current state-of-the-art, the methods adopted for direct measurements of short crack initiation & propagation are divided into three distinct categories.

The first approach is based on the post-inspection of broken specimens once the fatigue experimentation is over [12,13]. While this approach provides valuable insights on the location of crack initiation, it fails to precisely capture the evolution of fatigue cracks across different length scales. Moreover, such methods can only be employed after the specimen is broken, and are, therefore, always reactive. The second approach involves the utilization of different sensing devices (e.g., ultrasonic [11], acoustic emissions [14], and eddy currents [15]) that need to be calibrated using digital or optical microscopes. After calibration, the signal data obtained from the sensing devices are processed

* Corresponding author.
E-mail address: aub1526@psu.edu (A. Basak).

https://doi.org/10.1016/j.ijfatigue.2020.105922
Received 26 June 2020; Received in revised form 25 August 2020; Accepted 26 August 2020
Available online 30 August 2020
0142-1123/ © 2020 Elsevier Ltd. All rights reserved.

Nomenclature

List of Abbreviations

ASTM	American Society for Testing and Materials
CT	Computer Tomography
HMM	Hidden Markov Modeling
LCI	Long Crack Initiation
NDT	Non-Destructive Testing
SCI	Short Crack Initiation
SEM	Scanning Electron Microscope
SIF	Stress Intensity Factor
STSA	Symbolic Time Series Analysis

List of Symbols

β	Geometry factor
β_{long}	Geometry factor for long crack regime
β_{short}	Geometry factor for short crack regime
$\Delta\sigma$	Stress range
$\Delta\sigma_e$	Fatigue endurance limit
σ_{min}	Minimum stress
σ_{max}	Maximum stress
ΔK	Stress intensity factor
ΔK_{th}	Threshold stress intensity factor
ΔK_{th0}	Threshold stress intensity factor for stress ratio = 0
$\Delta K_{transverse\_long}$	Stress intensity factor for long transverse crack
$\Delta K_{transverse\_short}$	Stress intensity factor for short transverse crack
$a_{lateral}$	Lateral crack length
$a_{transverse}$	Transverse crack length
$a_{transverse\_long}$	Transverse crack length in the long crack regime
$a_{transverse\_short}$	Transverse crack length in the short crack regime
C	Material coefficient in the Paris' law
F_{max}	Maximum loading
K_t	Stress concentration factor
l_0	Length at which short crack starts growing
N	Number of cycles
m	Material coefficient in the Paris' law
R	Stress ratio
$t_{lateral}$	Lateral crack thickness
$t_{transverse}$	Transverse crack thickness

using sophisticated pattern recognition methods such as symbolic time series analysis (STSA) [16] and hidden Markov modeling (HMM) [17] to pinpoint the epoch of short crack initiation. The identification of events with such methods can be termed as passive because of their indirect communication with the crack. Due to the relative ease in employing such techniques, several sensing methods have been used in the past [18–23]. One of the primary issues with this approach is that the sensors cannot successfully pinpoint the short crack initiation at the micron scale. Hence, although these methods do not involve any expensive instrumentation like computed tomography (CT), microstructurally short cracks cannot be effectively captured using these techniques.

The third and final approach is to use a fatigue tester inside a CT [24–26] or a scanning electron microscope (SEM) [27,28] as shown in Fig. 2. However, the state-of-the-art testing apparatuses that can be installed inside the CT or SEM are limited by the frequency of load cycles and the peak load. A maximum of 10 Hz [29] has been reported in the literature for *in-situ* SEM while, for *in-situ* CT, the frequency is of order 50 Hz [24]. The specimen size is also a major concern as most of the stages are limited to miniaturized specimens of less than 50 mm in length [29], and therefore, restricting the ability to investigate large-scale specimens that typically show radically different fatigue-failure mechanisms compared to small specimens [30]. Additionally, for *in-situ* SEM, the crack initiation & propagation phenomena can always be observed on a single surface. Much of the existing literature has monitored the crack initiation at the side surfaces though it has been widely reported that crack originates invariably at the notch root (assuming that both notch and side surfaces have statistically similar roughness properties) [31].

Several other hybrid methods also exist in the open literature. An example of such a hybrid method is the implementation of sequential fatigue testing and CT measurements to characterize short crack initiation & propagation behavior [32]. However, when the specimen is unmounted for inspection and remounted for testing, both test continuity and the result integrity are compromised. In another example, the fatigue specimens are cyclically loaded to initiate a crack using a servo-hydraulic MTS load-frame, and, thereafter, the specimens are fatigue-tested inside a synchrotron [33]. Being restricted to either a smaller or larger specimen size is one of the critical drawbacks of the existing methods. For example, the ultrasonics are capable of detecting cracks at a length scale of millimeters [34], whereas a CT or an SEM can detect at a scale of micrometers. However, a measurement device that captures the behavior at multiple length-scales without being restricted to small or large specimens is currently lacking in the open literature. Table 1 summarizes the current capabilities of the state-of-the-art

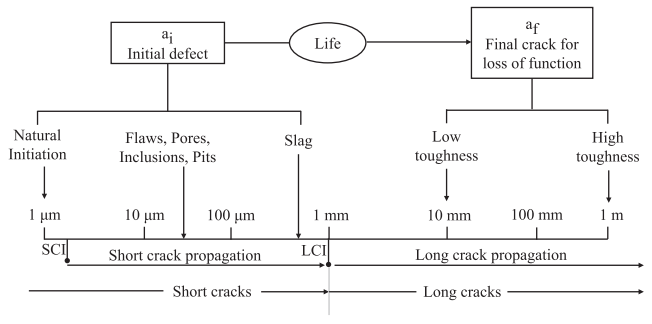

Fig. 1. Schematic showing the crack size scale for initial and final cracks (adopted from [7]). The initial crack length varies from 1 μm to ~ 1 mm, depending on the defects existing in the material. The final crack length is in the ranges of few millimeters. The boundary between long and short cracks is sometimes taken as ~1 mm in length. In the present work, a length scale of 1 mm is used to approximately discriminate short and long cracks. SCI = Short Crack Initiation and LCI = Long Crack Initiation.

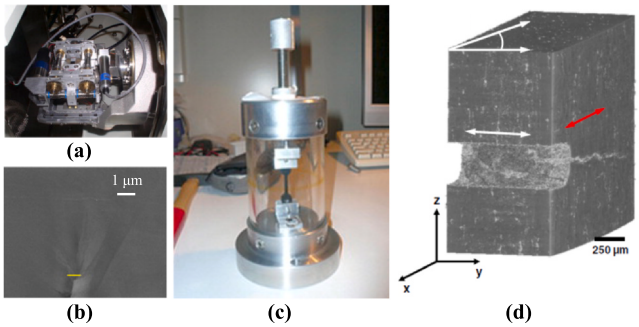

Fig. 2. (a) and (b) A representative *in-situ* fatigue testing apparatus inside an SEM and a sample result of fatigue crack detection, respectively (reproduced with permission from [28]), (c) a representative *in-situ* fatigue testing apparatus that can be installed inside a CT (reproduced with permission from [25]), and (d) a sample result of fatigue crack detection (reproduced from [26] under the terms of the Creative Commons Attribution 4.0 International License from http://creativecommons.org/licenses/by/4.0/).

Table 1
Current capabilities of the measurement setups – traditional, *in-situ* CT, and *in-situ* SEM. The capabilities are split into three categories, viz. experimental setup, short crack regime and long crack regime. The green tick implies the setup is equipped to handle the corresponding capability, whereas the green tick accompanied by a red star implies that the setup has a limited capability (e.g., a CT stage can handle a maximum crack length of ~3 mm). The red cross implies the shortcoming of the setup. NDT implies "Non-Destructive Testing".

			Testing Setup		
			Traditional (Fractography)	*In-situ* CT	*In-situ* SEM
Capability	Experimental setup	Flexibility with maximum loading	✓	×	×
		Flexibility with loading frequency	✓	×	×
		Flexibility with specimen size	✓	×	×
		Suitable for instrumenting with multiple *in-situ* NDT-based sensors	✓	×	×
	Short crack regime	Short crack initiation as a function of # of cycles at internal defects	×	✓	×
		Short crack initiation as a function of # of cycles at surface defects (single surface)	×	✓	✓
		Short crack initiation as a function of # of cycles at surface defects (multiple surfaces)	×	✓	×
		Short crack propagation pathways with # of cycles for internal cracks	×	✓	×
		Short crack propagation pathways with # cycles for surface cracks (single surface)	×	✓	✓
		Short crack propagation pathways with # cycles for surface cracks (multiple surfaces)	×	✓	×
	Long crack regime	Long crack initiation as a function of # of cycles at internal defects	×	✓	×
		Long crack initiation as a function of # of cycles at surface defects (single surface)	×	✓	✓
		Long crack initiation as a function of # of cycles at surface defects (multiple surfaces)	×	✓	×
		Long crack propagation pathways with # of cycles for internal cracks	×	✓*	×
		Long crack propagation pathways with # cycles for surface cracks (single surface)	×	✓*	✓*
		Long crack propagation pathways with # cycles for surface cracks (multiple surfaces)	×	✓*	×

measurement methods and identifies their limitations.

This paper presents an alternative technique to investigate and characterize both short and long crack initiation & propagation in Al7075-T6 (Al7075) notched specimens by using a confocal microscope and a digital microscope simultaneously during the fatigue tests. The confocal microscope is capable of detecting cracks at a length scale of 3 μm and higher, whereas the digital microscope can reliably measure cracks in the order of ~0.5 mm and higher. Thus, the present method characterizes both short and long crack initiation & propagation behavior for length scales ranging from 3 μm to 20 mm (width of the specimen). Moreover, taking advantage of multiple imaging capabilities, the present work illustrates the crack growth behavior along the thickness and width of the specimens simultaneously. To the best of the authors' knowledge, such a study is not available in the open literature. The observations are, therefore, first of its kind. The paper is organized into four sections including the present one. The experimental section outlines the material, specimen design, fatigue test apparatus, and the imaging procedure for both microscopes. It is followed by the results section which shows three important outcomes: a linear correlation between crack dimensions in the lateral and transverse directions, an estimation of the stress intensity factor (SIF), and the relative contributions of short and long cracks to the total fatigue life. Finally, the article summarizes the major conclusions and proposes future work with the newly developed experimental apparatus.

2. Experimental

2.1. Material and specimen

An investigation of the relative importance of surface features that govern the short and long crack initiation & propagation in Al7075 is crucial in naval and aviation applications. Al7075 is extensively used in aerospace structures due to its excellent mechanical properties (Table 2 [35]). Sheets of cold-rolled and hardened Al7075 are acquired from McMaster-Carr [36]. The specimens are extracted from a 2.286 mm (0.09″) thick Al7075 sheet using water jet machining to avoid the formation of residual stresses at the notch tip [37]. The geometrical details of the specimens are given in Fig. 3(a). The specimens follow the ASTM standard E466 [38] outlined for fatigue testing. The V-notch with a depth of 4 mm and a base radius of 0.5 mm is designed to create a high stress concentration factor (K_t=7) motivated by the aerospace and offshore applications [39]. The stress concentration factor is verified using a readily available finite-element based static simulation using the SolidWorks suite [40] as shown in Fig. 3(b). Additionally, fatigue simulations are performed using the SolidWorks simulation suite to verify that the notch region has the lowest life. Fig. 3(c) shows a fatigue simulation showing the corresponding total expected life of the component. The objective of the fatigue simulation is to computationally verify that the location with the minimum life corresponds to the notch region in an ideal scenario, thus ensuring the origin of the crack from a geometrical perspective. Among the two simulations shown, the static test provides a basis for the calculation of stress concentration and the fatigue test provides the information on total life. To that end, the simulation assumes an isotropic linear material for Al7075-T6 (from SolidWorks library) and does not incorporate any correction factors (e.g., surface roughness).

2.2. Fatigue testing

The specimens are subjected to a constant amplitude of uniaxial tensile loading with maximum loading, F_{max}=4 kN and the stress ratio, $R = 0.5(\sigma_{min}/\sigma_{max})$ at a frequency of 20 Hz. The tests have been performed on an MTS Elastomer 831.10 servo-hydraulic setup (Fig. 4) rated at a maximum load of 25 kN. The grips are acquired from TEST-RESOURCES (Shakopee, Minnesota, USA). The loads lead to a stress amplitude of 56 MPa and a maximum stress of 112 MPa at the notch root due to stress concentration. Existing literature reports that Al7075 specimens with a sharp V-notch show a fatigue life of around 54,000 cycles at room temperature with the following conditions: stress ratio of

Table 2
Material properties of Al7075 [35].

Property	Magnitude
Ultimate Tensile Strength (MPa)	572
Tensile Yield Strength (MPa)	503
Fatigue Strength (MPa)	159
Fracture Toughness (L-T) -(MPa. $m^{1/2}$)	29

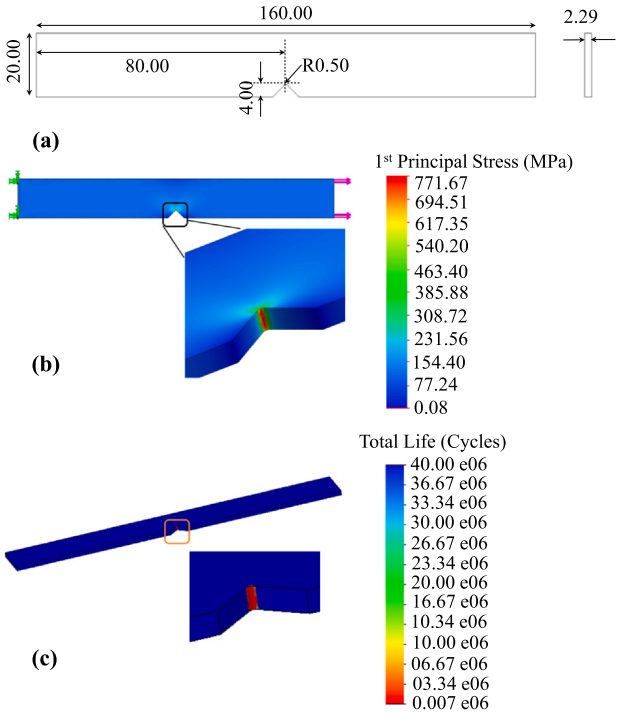

Fig. 3. (a) Geometry of the fatigue specimens (all dimensions are in mm). (b) Contour of the first principal stress in the designed specimen using the SolidWorks static simulation suite. (c) Fatigue simulation showing the contour of the total life using the SolidWorks simulation suite.

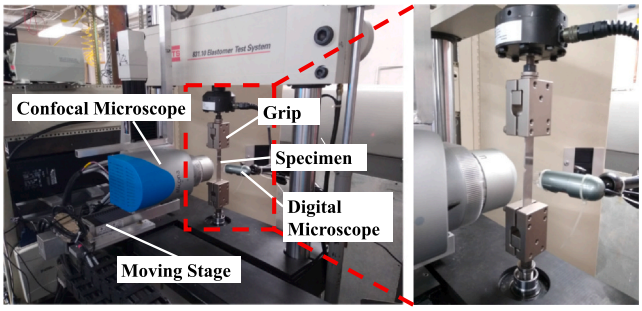

Fig. 4. (a) A custom-designed fatigue testing apparatus showing the MTS Elastomer 831.10 servo hydraulic frame, the digital microscope, the confocal microscope, and the moving stage on which the confocal microscope is mounted. (b) Zoomed view of the apparatus.

0.1, loading frequency of 20 Hz, stress amplitude of 31.5 MPa, and maximum stress of 70 MPa [41]. In the current study, the stress amplitude is increased to 56 MPa to reduce the life of the specimens as the custom fatigue testing involving capturing the necessary images takes a considerably long period of time. However, it is also ensured that a continuous collection of damage evolution data at a regular interval is obtained. The tests are performed using a routine in the Multi-Purpose TestWare™ software suite for the MTS controller. The routine enables a desired programmed periodical stops to facilitate imaging without unloading the specimens. To maintain test integrity, these stops are always made at the maximum load at every 500 cycles for all specimens reported in the present work.

2.3. Dual-imaging setup

During the test, the fatigue damage evolution is monitored along the lateral (i.e., the thickness of the specimens) as well as the transverse

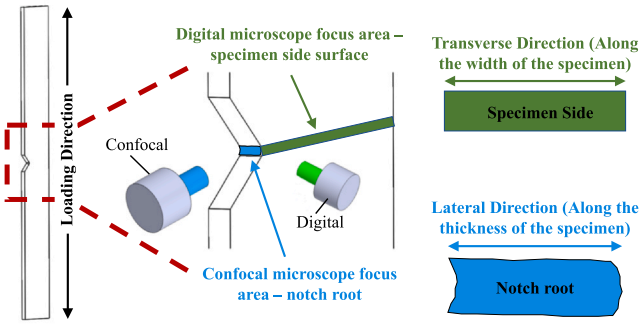

Fig. 5. (a) A schematic of the dual-imaging setup showing the placement of the cameras to characterize short and long crack initiation & propagation along the thickness and width of the specimens, respectively. (b) The reference directions used in this paper to characterize the lateral and transverse propagation directions.

(i.e., the width of the specimens) direction using a confocal and a digital microscope, respectively (Fig. 5). The confocal microscope is focused inside the notch while the digital microscope is focused on the side of the specimens. The confocal microscope with its superior resolution has a short crack detection capability of 3 μm, whereas the digital microscope can detect long crack initiation at roughly 0.5 mm. In this way, the setup ensures crack monitoring effectively at two different length scales. The main advantage of such a two-sided imaging study is the augmentation of the traditional long crack initiation & propagation capability with a precise short crack initiation & propagation detection without having any specimen geometry or testing frequency restriction. In this regard, the testing method developed in this work is scalable to any load and frequency.

2.3.1. Confocal microscope image acquisition

The confocal microscope used for the study is an Alicona IF-SensorR25 model. The microscope is manufactured by Bruker Alicona (Graz, Austria) and belongs to the InfiniteFocus series which uses a novel focus variation technology as schematically shown in Fig. 6 [42].

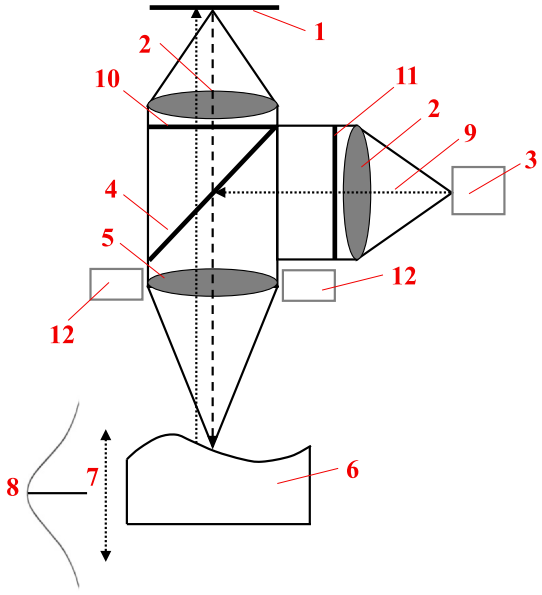

Fig. 6. Schematic diagram of a typical Confocal measurement device based on focus variation. 1. array detector, 2. lenses, 3. white light source, 4. beam splitter, 5. objective, 6. specimen, 7. vertical scan, 8. focus curve, 9. light beam, 10. analyzer, 11. polarizer, 12. ring light. This figure is reproduced with permission from [42].

It can capture a sharp image across the depth of the field through pixel by pixel calculation of image focus. The ring light illumination scheme in the instrument helps in measuring slopes up to 80° unlike other coaxial illumination techniques [43]. With the settings used during the experiment, the captured image has a vertical resolution of 20 nm and can detect crack initiation larger than roughly 3 μm. The microscope uses a customized software IF-MeasureSuite for capturing images and analyzing them.

The confocal microscope is set up to operate at 50X resolution while capturing an area of 400 μm × 400 μm (Fig. 7(a)). Since the microscope can capture a maximum length of 0.4 mm, it needs to be moved along the root of the notch to capture the entire root area (recall that the specimen is 2.29 mm thick, and hence, a total of 2.29/0.4 ≈ 6 images are required to cover the root area as shown in Fig. 7(b)). This is enabled by mounting the microscope on an Aerotech (Aerotech, Inc., Pittsburgh, USA) high-precision moving stage without which it would not be possible to monitor the short crack initiation & propagation behavior. The stage maintains precise control of movement up to the micrometer scale which enables efficient feature tracking. At every predefined interval, when the MTS machine pauses at the highest load (4 kN), the confocal microscope is made to scan through the entire root of the notch, and images at specific points are collected. At the beginning of the test when there is no crack growth, the root of the notch is imaged entirely. However, once the test starts, to minimize the duration of the pause for the purpose of having stress buildup in the specimens, the entire root area is scanned at all points and images are taken only at locations where crack initiation is observed. The dimension of a crack is measured by manually selecting the ends of a crack using the image processing toolbox in MATLAB®. The relative pixels in this selection are then compared with those of the known width of the image to extract the crack dimension. In the future, sophisticated image processing algorithms will be implemented for automatic extracting of crack dimensions from microscopic images [44].

2.3.2. Digital microscope image acquisition

The Dino-Lite Premier is a commonly used PC-based USB digital microscope for observing the macroscopic phenomenon [45,46]. In the context of this study, the digital microscope is focused on the side of the specimen (Fig. 4) such that any change in crack length can be captured. As mentioned in the previous section, the MTS system is programmed to stop at regular intervals to monitor the notch region. Due to the ease of capturing an image with this microscope, data is collected at every pause in the loading, unlike the confocal microscope which is just scanned during each stop and image taken at intermittent intervals. Fig. 7(c) illustrates a representative image obtained from the microscope showing a long crack. The camera comes with a fully equipped image processing tool called DinoCapture 2.0: Microscope Imaging Software which is used to measure the length of the cracks. The microscope can be used reliably in regions where the crack length reaches the length of around 0.5 mm, thus making it suitable for analyzing long cracks.

3. Results and discussion

3.1. Characterization of short and long crack initiation & propagation

Fatigue testing is conducted on five Al7075 specimens and the image data are collected. Fig. 8 shows the evolution of both short and long crack as observed by the confocal and digital microscopes, respectively. The total fatigue life of this specimen is 25,000 and at N = 12,000 (here, N = number of cycles), a short crack of thickness ~ 3 μm ($t_{lateral}$) appears at the notch root. However, the digital microscope does not detect anything at N = 12,000. In fact, the digital microscope only starts detecting the first sign of fatigue distress at around N = 24,000 when $a_{transverse}$ = 0.3 mm and $t_{lateral}$ = 8 μm. At around N = 34,000, the crack inside the notch is fully open from one side to the other.

3.2. Relationship between lateral and transverse crack dimensions

The thickness of the crack inside the notch play a critical role as this crack needs to propagate to the side of the specimens before any signs of damage or distress is observed on the side surfaces. A comparison of the $t_{lateral}$ and $a_{transverse}$ is shown in Fig. 9. When N < 15,000, due to better measurement resolution by the confocal microscope, the short crack initiation can be detected at a much earlier instant by observing $t_{lateral}$ as compared to $a_{transverse}$. The observed $t_{lateral}$ values are in the range of ~3 μm. On the other hand, reliable observations of long crack length from the digital microscope are greater than $a_{transverse}$ = 0.5 mm. Due to such contrast between the capabilities of the microscopes, it is inferred that $t_{lateral}$ values are useful to study the short-crack propagation behavior while $a_{transverse}$ values are conducive to analyze the long crack propagation behavior. It is assumed that long crack takes dominance between 1 and 2 mm [47] whereas any cracks below 1 mm would be considered as short crack. Based on this observation, in this work, a crack below 1 mm in length is considered a short crack.

The readers may wonder the reasons behind the absence of an equivalent $a_{transverse}$ vs. N and $a_{lateral}$ vs. N figures. While performing the fatigue experiments, at least 2 specimens showed multiple crack initiations inside the notch as illustrated in Fig. 10. In such cases, as some of these cracks appeared one above the other, it was quite ambiguous to calculate $a_{lateral}$. However, it turns out that the dominant crack shows the largest thickness and, hence, for all such cases, Fig. 9 reports the maximum $t_{lateral}$ observed. A regression model is fitted between $a_{transverse}$ and $t_{lateral}$ using the values from both microscopes for the cycles when both measurements are available for all five specimens. A linear regression model (R^2=0.8768) with the corresponding scatter plot of the measurements is shown in Fig. 11 and the fitted equation is:

$$a_{transverse} = f(t_{lateral}) = 0.0512 \times t_{lateral} - 0.0615 \quad (1)$$

where $a_{transverse}$ is in mm and $t_{lateral}$ in μm. Fig. 11 also shows the variation of ± 2σ (standard deviation) from a predictive distribution with no priors [48]. The linear model has a positive intercept on the x-axis indicating the emergence of short cracks along the lateral direction before the onset of a long crack along the transverse direction. Fitting a quadratic model barely changes the R^2 value to 0.88 with a very small

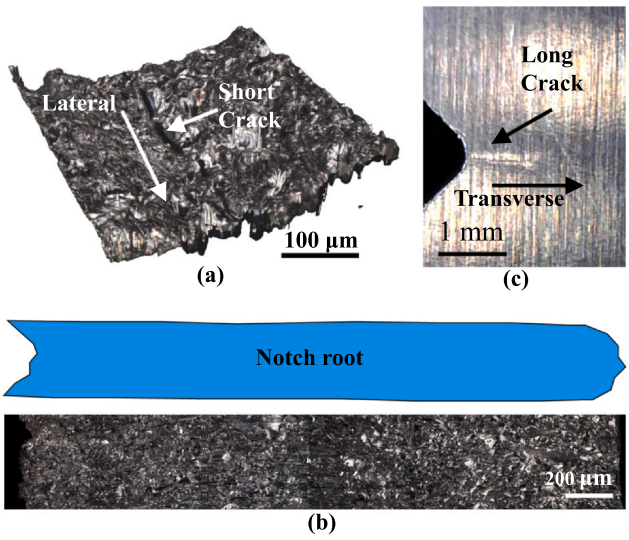

Fig. 7. (a) A representative image obtained from the confocal microscope showing a short crack. (b) An ensemble of six confocal images to cover the entire notch root. (c) A representtaive image obtained from the digital microscope.

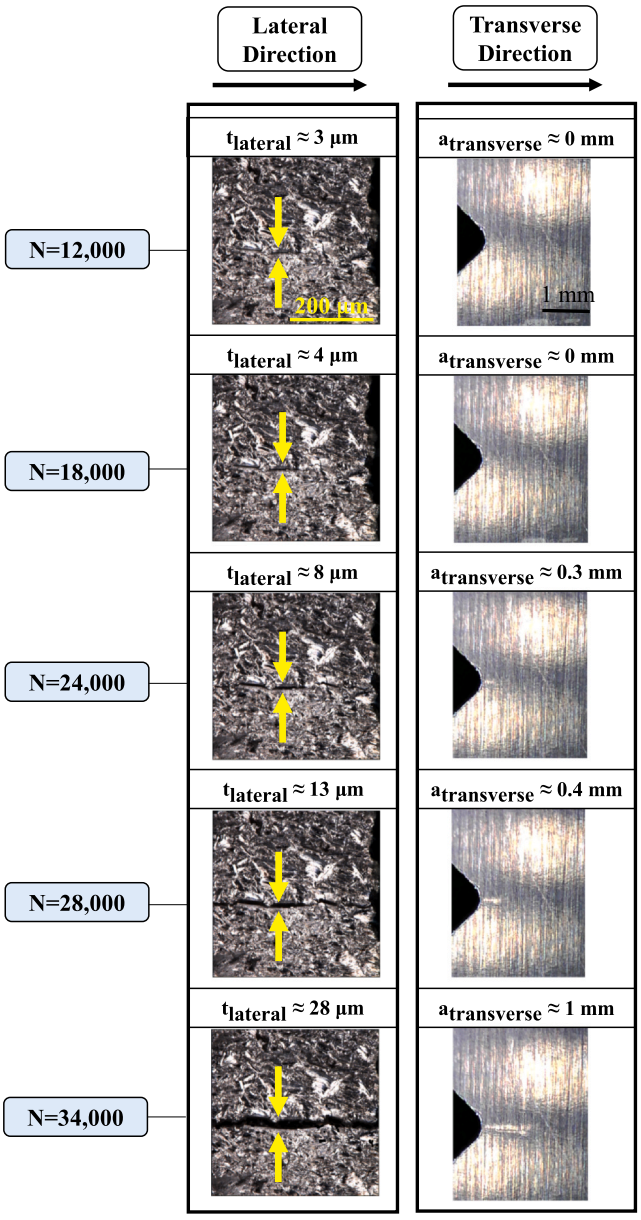

Fig. 8. Evolution of fatigue crack initiation and propagation as observed by the confocal microscope (left panel) and the digital microscope (right panel). Here, N represents the number of cycles, $t_{lateral}$ represents the thickness of the short crack along the lateral direction, and $a_{transverse}$ represents the length of the long crack along the transverse direction.

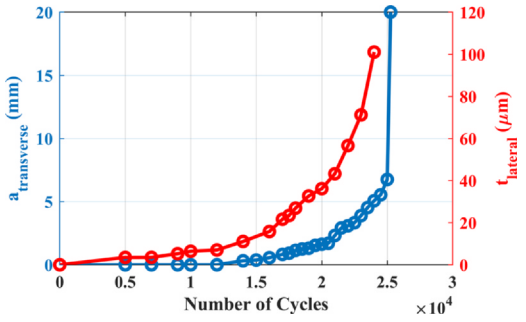

Fig. 9. Evolution of $a_{transverse}$ and $t_{lateral}$ with number of cycles for one Al7075 specimen. Other specimens also show similar behavior and they are skipped for brevity.

coefficient of the quadratic term effectively rendering it as a linear model. Therefore, for the current data, the simpler linear model is adequate.

The limitations of this regression model can be interpreted using the Paris' law [49] in the following way: $a_{transverse} = f(t_{lateral}) = \int C\Delta K^{m}_{transverse} dN$. Here, C and m are material constants. $\Delta K_{transverse}$ is the stress intensity factor in the transverse direction and N is the number of cycles. Since both $a_{transverse}$ and $f(t_{lateral})$ are seen to be dependent on C, m, $\Delta K_{transverse}$, and N via a nonlinear relationship, the statistical relation can also be assumed to depend on these parameters and the subsequent factors that affect them. This dependence would, therefore, limit the linear model to the presently studied material (Al7075), the stress range, the notch geometry, and the width of the specimen. The dependencies, however, is difficult to predict analytically due to the nonlinear nature and, therefore, needs to be verified experimentally.

3.3. Short crack initiation along the transverse direction

The digital microscope can detect cracks along the transverse direction at a minimum resolution of 0.5 mm as stated previously. However, following the formulation from [8,50], an estimate of l_0, a fictitious length where short crack starts growing along the transverse direction can be calculated for Al7075 specimens:

$$l_0 = \frac{1}{\pi}\left(\frac{\Delta K_{th}}{\Delta \sigma_e}\right)^2 \tag{2}$$

Here, ΔK_{th} is the threshold stress intensity factor and $\Delta\sigma_e$ is the fatigue endurance limit. For Al7075, $\Delta\sigma_e = 176$ MPa [8], and ΔK_{th} is given by

$$\Delta K_{th} = \left(\frac{1-R}{1+R}\right)^{1/2} \Delta K_{th0} \tag{3}$$

where $\Delta K_{th0} = 2.3$ MPa·m$^{1/2}$ [8] and R = stress ratio. For R=0.5, the above equations yield l_0=0.018 mm or 18 μm. Although this formulation defines the threshold ΔK_{th} for a semi-circular notch, the prediction gives an estimate of the expected length scale that is dominant during short crack propagation. Unfortunately, the digital microscope with its minimum resolution of 0.5 mm is unable to detect the short crack initiation & propagation along the transverse direction. By using the relationship obtained in Equation (1) for $a_{transverse}$=0.018 mm, the value of $t_{lateral}$ = 1.55 µm. Again, this thickness value is beyond the Confocal microscope's ability to detect. Nevertheless, the calculation of l_0 allows the users to have a perspective on the resolution requirement of the microscope for detecting short crack propagation. For example, by using the results obtained as guidelines, the authors are currently working on replacing the digital microscope with a Questar traveling optical microscope that takes images with a resolution of 1 µm per pixel at 75 to 150 mm working distance.

3.4. Stress intensity factor estimation along the transverse direction

While the existing literature lists expressions for calculating stress intensity factor (SIF) values for simpler notches such as a U-notch or a sharp V-notch [51,52], no such relationships are readily available for a rounded V-notch. To calculate SIF, certain analytical approaches are proposed in literature [53–55], particularly by Carpinteri [55] and Lazzarin [53]. These approaches, however, are suitable under certain specimen geometry and not universal. For example, Carpinteri's equation is suitable for crack lengths that are very small than the notch base radius. Additionally, the equation only works if the ratio of the notch base radius to the width is 1/20. Therefore, to estimate the SIF for such a rounded V-notch, an inverse approach is employed by numerically deriving the SIF using the known elements of the Paris equation [49] for crack growth. The commonly used Paris' law for crack growth is:

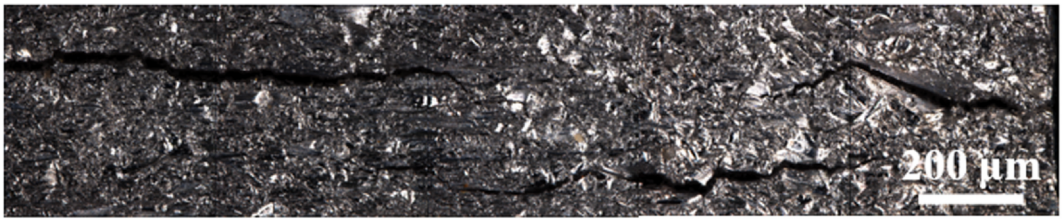

Fig. 10. A representative image showing multiple crack initiations inside the notch at N = 24,000.

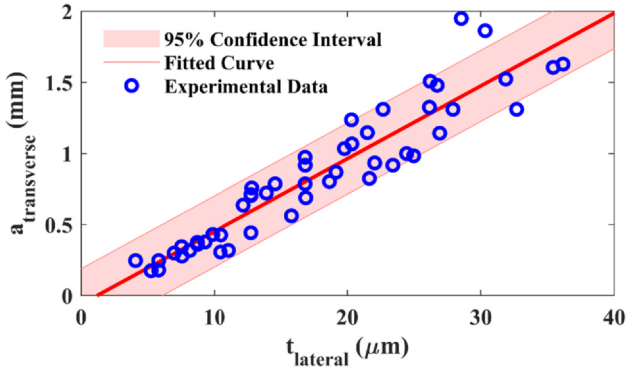

Fig. 11. Variation of $a_{transverse}$ with $t_{lateral}$ for all specimens.

$$\frac{da_{transverse}}{dN} = C(\Delta K_{transverse})^m \quad (4)$$

Here $a_{transverse}$ is the crack length in the transverse direction, N is the number of cycles, $\Delta K_{transverse}$ is the SIF, and C and m are material constants. From previous studies on Al7075, multiple resources have reported the values for C and m [8,56], where $\ln C = -21.189$ and $m=2.724$. Using these values, and numerically computing the crack growth rate, the SIF is evaluated using the relation:

$$\Delta K_{transverse} = \left[\frac{1}{C}\left(\frac{da_{transverse}}{dN}\right)\right]^{\frac{1}{m}} \quad (5)$$

ΔK can also be expressed using the geometry factor β [51]:

$$\Delta K_{transverse} = \beta \cdot \Delta\sigma \cdot \sqrt{\pi a_{transverse}} \quad (6)$$

Here β is the geometry factor and $\Delta\sigma$ is the stress range. The geometry factor is dependent on the specimen design and crack shape, and therefore, contains information about the geometry in SIF. Due to the

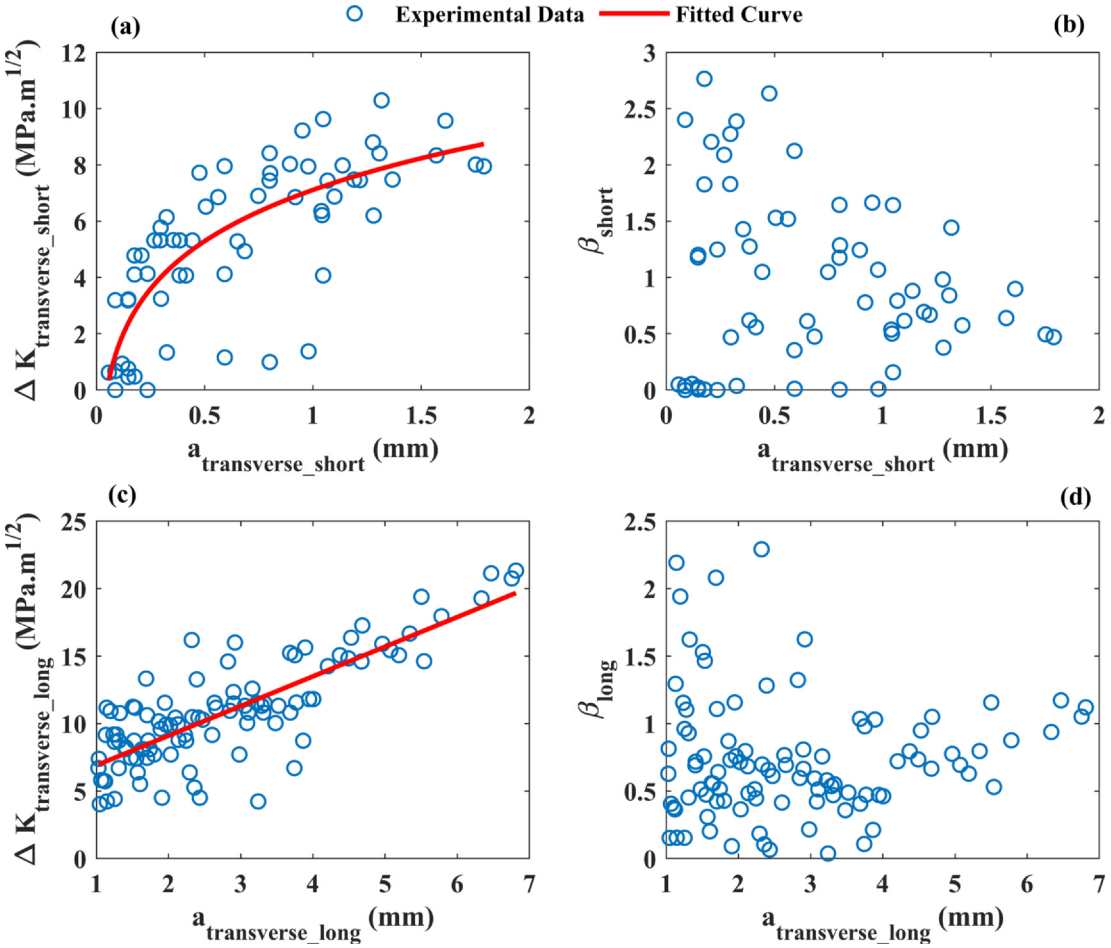

Fig. 12. Variation of (a) – (b) $\Delta K_{transverse\_short}$ (MPa·m$^{1/2}$) and β_{short} with $a_{transverse\_short}$ (mm), respectively; and (c) – (d) $\Delta K_{transverse\_long}$ (MPa·m$^{1/2}$) and β_{long} with $a_{transverse\_long}$ (mm), respectively. The data for all 5 specimens is represented under the "Experimental Data" together.

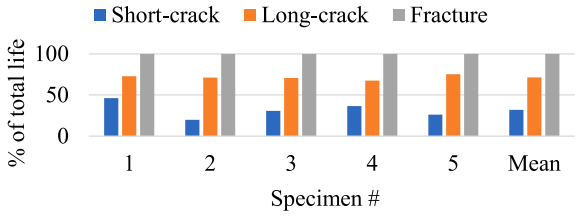

Fig. 13. Improvement in detection capability as a fraction of total fatigue life through the usage of confocal microscope.

multiscale nature of the crack measurements, the computation is split into two parts: SIF for the short crack regime along the transverse direction ($\Delta K_{transverse\_short}$) and SIF for the long crack regime along the transverse direction ($\Delta K_{transverse\_long}$). It is also assumed that for both regimes, the values of C and m are identical. Since, these parameters are "fitted" ones, they may not be correct for both short and long crack regimes. However, the analysis gives an avenue to estimate $\Delta K_{transverse\_short}$ and $\Delta K_{transverse\_long}$. With the availability of accurate fitting parameters, the estimation of $\Delta K_{transverse\_short}$ and $\Delta K_{transverse\_long}$ is poised to improve.

For the long crack regime, $a_{transverse\_long}$ and N values are readily available from the digital microscope. However, for the short crack regime, since the digital microscope data cannot be reliably used below 0.5 mm, the information from confocal microscope along with the transformation from the regression equation in Eq. (1) is used. In this formulation, the SIF for short crack regime is estimated up to a=1 mm. To incorporate the regression curve $a_{transverse}=f(t_{lateral})$, the Paris' law is modified using the chain rule as shown in Eq. (8). Two sets of equations are therefore available to calculate both $\Delta K_{transverse\_short}$ and $\Delta K_{transverse\_long}$, and β_{short} and β_{long}.

$$\frac{da_{transverse\_long}}{dN} = C(\Delta K_{transverse\_long})^m \tag{7}$$

$$\frac{da_{transverse\_short}}{dN} = \frac{df(t_{lateral})}{dt_{lateral}}\frac{dt_{lateral}}{dN} = C(\Delta K_{transverse\_short})^m \tag{8}$$

$$\Delta K_{transverse\_long} = \beta_{long}\cdot\Delta\sigma\cdot\sqrt{\pi a_{transverse\_long}} \tag{9}$$

$$\Delta K_{transverse\_short} = \beta_{short}\cdot\Delta\sigma\cdot\sqrt{\pi a_{transverse\_short}} \tag{10}$$

The derivatives are calculated using a finite difference scheme [57]. No interpolation between the available data is used. The results for $\Delta K_{transverse}$ (both short and long) and β (both short and long) as functions of crack length (both short and long) are shown in Fig. 12. The variation of $\Delta K_{transverse\_short}$ for the transverse cracks follows a power curve: $\Delta K_{transverse\_short} = 26.79 \times a_{transverse\_short}^{0.1015} - 19.68$ whereas $\Delta K_{transverse\_long}$ varies linearly with the crack length: $\Delta K_{transverse\_long} = 2.197 \times a_{transverse\_long} + 4.714$. Here, $\Delta K_{transverse\_short}$ and $\Delta K_{transverse\_long}$ are in $MPa.m^{1/2}$ and $a_{transverse\_short}$ and $a_{transverse\_long}$ are in mm. The variation for β, on the other hand, is noisy for both regimes (e.g., long and short) and does not show any functional forms. It is, therefore, obvious not to use a constant β value while analyzing the crack propagation behavior for short and long cracks. To emphasize further, the data in Fig. 12(a) and (b) is computed using the information from the confocal microscope and the data in Fig. 12(c) and (d) is computed using the digital microscope. Although the demarcation between the short and long cracks is assumed to be 1 mm, the prediction of the SIF in the short crack regime is extended to 2 mm in Fig. 12(a) to investigate if an overlap exists between the short and long crack regime (i.e., between 1 and 2 mm). It is observed that the tail end prediction obtained from Fig. 12(a) is remarkably similar the SIF computation from the initial region of the long crack regime (Fig. 12(b)) even with different models (Eqs. (7) and (8)). Since the data reported in Fig. 12(a) and (c) are from independent sources (i.e., confocal, and digital, respectively), the synchrony in these observations bolster the credibility of the reported results.

3.5. Fatigue life in short and long crack regimes

A critical outcome of the dual-imaging methodology is the comparison of the number of cycles at which the short crack starts to initiate along the lateral direction as compared to the long crack initiation along the transverse direction. The short crack growth is assumed to be initiated when the confocal microscope detects a crack of thickness roughly equaling 3 μm inside the notch. However, as specified earlier, the digital microscope detects a short crack along the transverse direction at the minimum resolution of 0.5 mm. This augmented capability of detecting a crack at micron scale is used to calculate the fatigue life prediction capability as a fraction of total life for all five specimens as shown in Fig. 13. The bar chart reflects that, on an

Table 3
Comparison of the existing capabilities with the newly developed testing procedure. The capabilities are split into three categories, viz. experimental setup, short crack regime and long crack regime. The green tick implies the setup is equipped to handle the corresponding capability, whereas the green tick accompanied by a red star implies that the setup has a limited capability (e.g., a CT stage can handle a maximum crack length of ~ 3 mm). The red cross implies the shortcoming of the setup.

			Testing Setup			
			Traditional (Fractography)	*In-situ* CT	*In-situ* SEM	Current Work
Capability	Experimental setup	Flexibility with maximum loading	✓	✗	✗	✓
		Flexibility with loading frequency	✓	✗	✗	✓
		Flexibility with specimen size	✓	✗	✗	✓
		Suitable for instrumenting with multiple *in-situ* NDT-based sensors	✓	✗	✗	✓
	Short crack regime	Short crack initiation as a function of # of cycles at internal defects	✗	✓	✗	✗→✓
		Short crack initiation as a function of # of cycles at surface defects (one surface only)	✗	✓	✓	✓
		Short crack initiation as a function of # of cycles at surface defects (multiple surfaces)	✗	✓	✗	✓
		Short crack propagation pathways with # of cycles for internal cracks	✗	✓	✗	✗→✓
		Short crack propagation pathways with # cycles for surface cracks (one surface only)	✗	✓	✓	✓
		Short crack propagation pathways with # cycles for surface cracks (multiple surfaces)	✗	✓	✗	✓
	Long crack regime	Long crack initiation as a function of # of cycles at internal defects	✗	✓	✗	✗→✓
		Long crack initiation as a function of # of cycles at surface defects (one surface only)	✗	✓	✓	✓
		Long crack initiation as a function of # of cycles at surface defects (multiple surfaces)	✗	✓	✗	✓
		Long crack propagation pathways with # of cycles for internal cracks	✗	✓*	✗	✗→✓
		Long crack propagation pathways with # cycles for surface cracks (one surface only)	✗	✓*	✓*	✓
		Long crack propagation pathways with # cycles for surface cracks (multiple surfaces)	✗	✓*	✗	✓

average, the confocal microscope can detect the short crack propagation inside the notch along the lateral direction as early as ~32% (standard deviation 9%) into the total fatigue life whereas the digital microscope can detect the long crack propagation along the transverse direction at around ~72% (standard deviation 2.5%) of the fatigue life under the given loading conditions. This comparison presents yet another important outcome of the current methodology which can prove extremely beneficial for prognostics research.

4. Summary, conclusion, and future work

The paper demonstrates a novel methodology to study fatigue crack initiation & propagation on a dual-imaging apparatus that is built upon consisting of a confocal microscope and a digital microscope, each of which is computer-instrumented and computer-controlled. The confocal microscope is used to capture the short crack initiation & propagation inside the notch while the digital microscope is used to detect long crack initiation & propagation along the width of the specimens. The integration of the data collected from these two microscopes reveals that there exists a linear relationship between the crack thickness along the lateral direction and crack length along the transverse direction. Fatigue cracks initiate at the root of the notch and propagates along the lateral direction until it reaches the side surface. Hence, beginning of the damage, the side surfaces may or may not show any signs of fatigue distress depending on where the crack initiates inside the notch (i.e., the relative location of crack initiation with respect to the side surface). This observation, though intuitive, allows for the calculation of two different SIFs, respectively for short and long crack propagation along the transverse direction. Additionally, with the current experimental apparatus, the short crack initiation is detected when the specimen approaches ~32% of its fatigue life, whereas with the long crack initiation is detected at ~72% of the fatigue life. Overall, the framework successfully fills the gaps in the existing crack detection methods without having any restrictions with regards to specimen size and loading conditions as shown in Table 3.

The current framework reveals the onset of fatigue failure through the development of multiple short cracks with one of them leading to the final failure. Detecting such multiple short cracks and observing their propagation is an additional advantage with the current setup. However, it is not obvious from the limited experimental data the physics behind such multiple crack initiation. A good way to explain this phenomenon is possible using sophisticated computational modeling which is currently being pursued [58]. In the future, several specimens with different notch surface roughness will be simulated and experimentally validated to investigate the local stresses generated as functions of surface roughness. Additionally, as indicated in Table 3, the current work is not equipped to detect crack initiation at internal defects in a straightforward way. However, this drawback can be potentially mitigated by pre-processing the specimens with CT to identify defects at the gauge section of a representative specimen. Suitable computational modeling techniques incorporating uncertainty analysis will be applied to identify the location of the defects that will act as a crack initiation site. The confocal microscope will be focused at this location with a bounding area of 400 μm × 400 μm. The initiation of fatigue crack at internal defects is expected to alter the surface features that will reflect in the fractal roughness measurements of the surface even before the crack reaches the surface [31]. Such surface features will be captured by the confocal microscope to pinpoint crack initiation.

In addition to the advantages of the setup, some cautionary measures should be considered with its usage. The resolution of the digital microscope at smaller length scales may cause errors in the measurement. This is, however, inherent to the measurement device and can be mitigated by using higher-resolution microscopes. From the measurement perspective, as mentioned before, crack lengths are measured using the DinoCapture 2.0 software that accompanies the digital microscope. The software has an intuitive interface and the measurements are easily repeatable with an accuracy of ± 0.08 mm based on the magnification used in the study. For the confocal microscope, the custom MATLAB® software needs the user to select the endpoints of the thickness of the crack from the images. The software provides an accuracy of ± 1 μm based on the pixel calculations. Assuming some variability in human intervention, the accuracies do not affect the statistical parameters seen in the regression model. Moreover, the 95% confidence interval shown in Fig. 11 should incorporate the effects of repeatability of measurements due to human intervention. In the future, more robust measurement techniques based on automated image processing algorithms [44], that require no human intervention, will be implemented.

Early detection of fatigue failures can be extremely beneficial while working with novel manufacturing technologies, such as additive manufacturing [59], which have sparse documentation of the desired performance. From the prognostics perspective, early detection of cracks can provide better corroborating measures for systems which use non-destructive testing (NDT)-based sensors for detection. Ultrasonics, acoustic emissions, eddy currents, and many such sensors provide an indication of fatigue damage, but the calibrating element in all such sensors is usually an imaging device which points to the exact occurrence of the crack [60,61]. The calibration of such sensors (or the algorithms therein) can be significantly affected with such imaging technique. With the growing interest in computer vision and its applications to prognostics, such methods can provide a repository for rich training images for deep learning [62] as well. In the future, this newly developed apparatus will be used to evaluate the fatigue properties of additively manufactured metallic specimens such as Inconel alloys.

Declaration of Competing Interest

The authors declare that they have no known competing financial interests or personal relationships that could have appeared to influence the work reported in this paper.

Acknowledgements

The work reported in this paper is supported in part by the Department of Mechanical Engineering at the Pennsylvania State University, University Park, PA 16802, United States. Any opinions, findings, and conclusions in this paper are those of the authors and do not necessarily reflect the views of the supporting institutions. The authors would also like to thank Kevin Fisher for his help with the MTS fatigue testing apparatus and the confocal microscope.

References

[1] Schütz W. A history of fatigue. Eng Fract Mech 1996;54(2):263–300.
[2] Liu Y, Ishihara T. Fatigue failure accident of wind turbine tower in Taikoyama wind power plant. Measurement 2015;15:20.
[3] Suresh S. Fatigue of materials. Cambridge University Press; 1998.
[4] Schijve J. Fatigue of structures and materials. Springer Science & Business Media; 2001.
[5] R.J. Asaro, Crystal plasticity, (1983).
[6] Gu T, Stopka KS, Xu C, McDowell DL. Prediction of maximum fatigue indicator parameters for duplex Ti–6Al–4V using extreme value theory. Acta Mater 2020;188:504–16.
[7] Tanaka K. Mechanics and micromechanics of fatigue crack propagation, Fracture mechanics: perspectives and directions (twentieth symposium). ASTM International; 1989.
[8] Amiri M, Modarres M. Short fatigue crack initiation and growth modeling in aluminum 7075–T6. Proc Instit Mech Eng, Part C: J Mech Eng Sci 2015;229(7):1206–14.
[9] Yu L, Tian Z. Lamb wave structural health monitoring using a hybrid PZT-laser vibrometer approach. Struct Health Monit 2013;12(5–6):469–83.
[10] Lankford J, Hudak Jr S. Relevance of the small crack problem to lifetime prediction

in gas turbines. Int J Fatigue 1987;9(2):87–93.
[11] Gupta S, Ray A. Real-time fatigue life estimation in mechanical structures. Meas Sci Technol 2007;18(7):1947.
[12] Nejad RM, Shariati M, Farhangdoost K. Prediction of fatigue crack propagation and fractography of rail steel. Theor Appl Fract Mech 2019;101:320–31.
[13] Goldsmith N, Wanhill R, Molent L. Quantitative fractography of fatigue and an illustrative case study. Eng Fail Anal 2019;96:426–35.
[14] Vanniamparambil P, Guclu U, Kontsos A. Identification of crack initiation in aluminum alloys using acoustic emission. Exp Mech 2015;55(5):837–50.
[15] Papazian JM, Nardiello J, Silberstein RP, Welsh G, Grundy D, Craven C, et al. Sensors for monitoring early stage fatigue cracking. Int J Fatigue 2007;29(9–11):1668–80.
[16] Gupta S, Ray A, Keller E. Symbolic time series analysis of ultrasonic data for early detection of fatigue damage. Mech Syst Sig Process 2007;21(2):866–84.
[17] Ling B, Khonsari M, Mesgarnejad A, Hathaway R. Online coated ball bearing health monitoring using degree of randomness and Hidden Markov Model. 2009 IEEE Aerospace conference. IEEE; 2009. p. 1–10.
[18] Kim J-Y, Yakovlev V, Rokhlin S. Surface acoustic wave modulation on a partially closed fatigue crack. J Acoustical Soc Am 2004;115(5):1961–72.
[19] Zilberstein V, Grundy D, Weiss V, Goldfine N, Abramovici E, Newman J, et al. Early detection and monitoring of fatigue in high strength steels with MWM-arrays. Int J Fatigue 2005;27(10–12):1644–52.
[20] Yamanaka K, Enomoto Y. Observation of surface cracks with scanning acoustic microscope. J Appl Phys 1982;53(2):846–50.
[21] Staszewski W, Lee B, Traynor R. Fatigue crack detection in metallic structures with Lamb waves and 3D laser vibrometry. Meas Sci Technol 2007;18(3):727.
[22] Sola JF, Kelton R, Meletis EI, Huang H. Predicting crack initiation site in polycrystalline nickel through surface topography changes. Int J Fatigue 2019;124:70–81.
[23] Wagner D, Ranc N, Bathìas C, Paris PC. Fatigue crack initiation detection by an infrared thermography method. Fatigue Fract Eng Mater Struct 2010;33(1):12–21.
[24] Buffiere J-Y, Maire E, Adrien J, Masse J-P, Boller E. In situ experiments with X ray tomography: an attractive tool for experimental mechanics. Exp Mech 2010;50(3):289–305.
[25] Cosmi F, Bernasconi A. Micro-CT investigation on fatigue damage evolution in short fibre reinforced polymers. Compos Sci Technol 2013;79:70–6.
[26] Singh SS, Williams JJ, Hruby P, Xiao X, De Carlo F, Chawla N. In situ experimental techniques to study the mechanical behavior of materials using X-ray synchrotron tomography. Integrating Mater Manuf Innov 2014;3(1):9.
[27] Andersson H, Persson C. In-situ SEM study of fatigue crack growth behaviour in IN718. Int J Fatigue 2004;26(3):211–9.
[28] Zhang W, Liu Y. Investigation of incremental fatigue crack growth mechanisms using in situ SEM testing. Int J Fatigue 2012;42:14–23.
[29] Qian G, Jian Z, Pan X, Berto F. In-situ investigation on fatigue behaviors of Ti-6Al-4V manufactured by selective laser melting. Int J Fatigue 2020;133:105424.
[30] Taylor D. Geometrical effects in fatigue: a unifying theoretical model. Int J Fatigue 1999;21(5):413–20.
[31] Jha DK, Singh DS, Gupta S, Ray A. Fractal analysis of crack initiation in polycrystalline alloys using surface interferometry. EPL (Europhysics Letters) 2012;98(4):44006.
[32] Withers PJ, Preuss M. Fatigue and damage in structural materials studied by X-ray tomography. Ann Rev Mater Res 2012;42:81–103.
[33] Waddell M, Walker K, Bandyopadhyay R, Kapoor K, Mallory A, Xiao X, et al. Small fatigue crack growth behavior of Ti-6Al-4V produced via selective laser melting: In situ characterization of a 3D crack tip interactions with defects. Int J Fatigue 2020;105638.
[34] Gupta S, Ray A, Keller E. Online fatigue damage monitoring by ultrasonic measurements: A symbolic dynamics approach. Int J Fatigue 2007;29(6):1100–14.
[35] A. International. http://asm.matweb.com/search/SpecificMaterial.asp?bassnum=MA7075T6.
[36] McMaster-Carr. https://www.mcmaster.com/aluminum-alloy-7075/high-strength-7075-aluminum-sheets-and-bars-7/.
[37] Boud F, Loo L, Kinnell P. The impact of plain waterjet machining on the surface integrity of aluminium 7475. Procedia Cirp 2014;13(2014):382–6.
[38] A. Designation, E466-07, Standard practice for conducting force controlled constant amplitude axial fatigue tests of metallic materials, ASTM International, 2007.
[39] N'diaye A, Hariri S, Pluvinage G, Azari Z. Stress concentration factor analysis for notched welded tubular T-joints. Int J Fatigue 2007;29(8):1554–70.
[40] Kurowski P. Engineering Analysis with SolidWorks Simulation 2013. SDC publications; 2013.
[41] Albedah A, Bouiadjra BB, Mohammed S, Benyahia F. Fractographic analysis of the overload effect on fatigue crack growth in 2024–T3 and 7075–T6 Al alloys. Int J Miner Metall Mater 2020;27(1):83–90.
[42] Danzl R, Helmli F, Scherer S. Focus Variation–a Robust Technology for High Resolution Optical 3D Surface Metrology. Strojniski Vestnik/J Mech Eng 2011;57(3).
[43] Gao W, Haitjema H, Fang F, Leach R, Cheung C, Savio E, et al. On-machine and in-process surface metrology for precision manufacturing. CIRP Ann 2019;68(2):843–66.
[44] Sosa J, Huber D, Welk B. Development and application of MIPAR™: a novel software package for two-and three-dimensional microstructural characterization. Integrat Mater Manuf Innovat 2014;3(1):10.
[45] Muaz M, Choudhury SK. Experimental investigations and multi-objective optimization of MQL-assisted milling process for finishing of AISI 4340 steel. Measurement 2019;138:557–69.
[46] Siddiqui SF, Fasoro AA, Cole C, Gordon AP. Mechanical Characterization and Modeling of Direct Metal Laser Sintered Stainless Steel GP1. J Eng Mater Technol 2019;141(3).
[47] Pearson S. Initiation of fatigue cracks in commercial aluminium alloys and the subsequent propagation of very short cracks. Eng Fract Mech 1975;7(2):235–47.
[48] Bishop CM. Pattern recognition and machine learning. Springer; 2006.
[49] P. Paris, F. Erdogan, A critical analysis of crack propagation laws, (1963).
[50] El Haddad M, Dowling N, Topper T, Smith K. J integral applications for short fatigue cracks at notches. Int J Fract 1980;16(1):15–30.
[51] Tada H, Paris P, Irwin G. The analysis of cracks handbook. New York: ASME Press; 2000. p. 1.
[52] Pilkey WD, Pilkey DF, Bi Z. Peterson's stress concentration factors. John Wiley & Sons; 2020.
[53] Lazzarin P, Filippi S. A generalized stress intensity factor to be applied to rounded V-shaped notches. Int J Solids Struct 2006;43(9):2461–78.
[54] Sapora A, Cornetti P, Carpinteri A. Analytical Stress Intensity Factors for cracks at blunted V-notches. Procedia Mater Sci 2014;3:738–43.
[55] Carpinteri A, Cornetti P, Sapora A. Brittle failures at rounded V-notches: a finite fracture mechanics approach. Int J Fract 2011;172(1):1–8.
[56] Kaynak C. Short fatigue crack growth in Al 2024–T3 and Al 7075–T6. Eng Fract Mech 1992;43(5):769–78.
[57] Zill D, Wright WS, Cullen MR. Advanced engineering mathematics. Jones & Bartlett Learning; 2011.
[58] Dinh TD, Vanwalleghem J, Xiang H, Erdelyi H, Craeghs T, Van Paepegem W. A unified approach to model the effect of porosity and high surface roughness on the fatigue properties of additively manufactured Ti6-Al4-V alloys. Addit Manuf 2020;33:101139.
[59] Basak A, Das S. Epitaxy and microstructure evolution in metal additive manufacturing. Annu Rev Mater Res 2016;46:125–49.
[60] Gupta S, Singh DS, Ray A. Statistical pattern analysis of ultrasonic signals for fatigue damage detection in mechanical structures. NDT and E Int 2008;41(7):491–500.
[61] Caesarendra W, Kosasih B, Tieu AK, Zhu H, Moodie CA, Zhu Q. Acoustic emission-based condition monitoring methods: Review and application for low speed slew bearing. Mech Syst Sig Process 2016;72:134–59.
[62] Wang S, Zhang P, Zhou S, Wei D, Ding F, Li F. A computer vision based machine learning approach for fatigue crack initiation sites recognition. Comput Mater Sci 2020;171:109259.